Journal of Materials Chemistry A

PAPER

View Article Online
View Journal | View Issue

Cite this: J. Mater. Chem. A, 2019, 7, 13096

Modular development of metal oxide/carbon composites for electrochemical energy conversion and storage†

Yuanchun Ji,‡[ab] Yuan Ma,‡[bc] Rongji Liu,[a] Yanjiao Ma,[bc] Kecheng Cao,[d] Ute Kaiser,[d] Alberto Varzi,[bc] Yu-Fei Song,*[e] Stefano Passerini*[bc] and Carsten Streb*[ab]

Received 2nd April 2019
Accepted 7th May 2019

DOI: 10.1039/c9ta03498f

rsc.li/materials-a

We report a convergent, modular materials design strategy, which gives access to multifunctional metal oxide/carbon composites for high-performance electrocatalysis and electrochemical energy storage. The materials design uses the thermal conversion of a metal organic framework (ZIF-67) functionalized with molecular vanadium oxide clusters ($[V_{10}O_{28}]^{6-}$) to give a nanostructured composite where redox-active crystalline Co–V–oxide nanoparticles (~5 nm) are firmly embedded in a high surface-area N-doped graphitic carbon matrix. The composite shows high activity, efficiency and stability for the electrocatalytic oxygen evolution reaction in alkaline conditions. In addition, proof of concept studies show fast and reversible Li storage behavior. Based on this new materials design principle, the divergent fields of electrocatalysis and battery materials design could be linked to enable a more efficient, converging materials design approach.

1. Introduction

Redox-active metal oxide/carbon composites play an essential role in future energy conversion and storage technologies such as batteries and water electrolysis.[1–3] On one hand, the development of cost-efficient oxygen evolution reaction (OER) electrocatalysts based on earth-abundant transition metal oxides is still a major challenge in materials chemistry. This is due to the significant obstacles associated with effective OER catalysts including the need for low overpotentials, long operational times and chemical stability under highly oxidative and corrosive conditions.[4–6]

On the other hand, both stationary and mobile batteries urgently need economically viable electrode materials, which combine high energy density and cycling stability with fast (dis-)charging capability. To-date, many commercial lithium-ion battery (LIBs) electrode materials suffer from relatively slow Li^+ ion diffusion. The number of charges stored per formula unit also need to be increased to reach the maximum theoretical energy densities.[7–9]

These different technologies share several common materials requirements such as redox-active sites, efficient interfacial charge-transport and high stability under chemically demanding conditions. Despite these common requirements, current energy materials design uses a divergent approach where materials are either developed for battery electrodes or for electrocatalysis.[10] Here, we propose a converging approach could potentially open new avenues for efficient and innovative materials design. By understanding the fundamental requirements of batteries and electrocatalysts, a joint materials design approach can be possibly leading to technologically relevant platform composites, which can subsequently be optimized for use in battery technologies as well as electrocatalysis.

One of the most promising approaches to this end is a modular bottom-up materials design where redox-active molecular metal oxide precursors (so-called polyoxometalates, POMs)[11] are incorporated into porous metal–organic frameworks (MOFs).[12] The beauty of this concept is the combination of POMs offering vast structural, chemical and redox-tunability,[13,14] with modular MOFs where ordered pores suitable for POM-uptake are combined with the presence of carbon-rich organic ligands as precursors for electrically conductive carbon nanostructures. In the context of high gravimetric energy density, reversible multi-electron storage and high redox-activity,[15] polyoxovanadates, *i.e.*, highly redox-active vanadium oxide clusters, are ideal prototypes.[16] Polyoxovanadates offer wide structural variability and chemical tunability,[16,17] so that

[a]Institute of Inorganic Chemistry I, Ulm University, Albert-Einstein-Allee 11, D-89081 Ulm, Germany. E-mail: carsten.streb@uni-ulm.de

[b]Helmholtz Institute Ulm (HIU), Helmholtzstrasse 11, D-89081 Ulm, Germany. E-mail: stefano.passerini@kit.edu

[c]Karlsruhe Institute of Technology (KIT), P.O. Box 3640, D-76021 Karlsruhe, Germany

[d]Central Facility for Electron Microscopy, Group of Electron Microscopy of Materials Science, Ulm University, Albert-Einstein-Allee 11, D-89081 Ulm, Germany

[e]Beijing Advanced Innovation Center for Soft Matter Science and Engineering, State Key Laboratory of Chemical Resource Engineering, Beijing University of Chemical Technology, Beijing, P. R. China. E-mail: songyf@mail.buct.edu.cn

† Electronic supplementary information (ESI) available. See DOI: 10.1039/c9ta03498f

‡ These authors contributed equally.

an additional redox-active transition metals can be incorporated in the cluster shell to modulate the electrochemical and electrocatalytic performance.[18–23] However, to the best of our knowledge, no POM-based systems have been reported which showed general activity in electrocatalysis as well as electrochemical energy storage. Over recent years, several strategies have been developed to directly incorporate POMs into MOF matrices, leading to hybrid host–guest composites.[24–27] In their native state, the performance of these composites is often hampered by low electrical conductivity, limited stability and poor catalytic performance. Pioneering studies to address these challenges have used the thermal conversion of the POM@MOF precursor into nanostructured solid-state compounds. In one striking example, Lou *et al.* have synthesized transition metal carbides (MoC_x) by pyrolysis of $[PMo_{12}O_{40}]^{3-}$@NENU-5 POM–MOF composites. The materials exhibit remarkable electrocatalytic hydrogen evolution performance combined with high stability in acidic and basic aqueous solutions.[28] In the field of LIB battery materials, Qiu *et al.* have simultaneously inserted $[PMo_{12}O_{40}]^{3-}$ and $[PW_{12}O_{40}]^{3-}$ into NENU-5. Pyrolysis of the material gave mixed Mo–W–Cu oxide/porous carbon composites which showed superb stability as LIBs anodes.[29]

2. Results and discussion

Here, for the first time, we report how one principal materials design approach gives access to a highly redox-active metal oxide/carbon composite, which shows activity for the electrochemical OER as well as electrochemical energy storage in LIB. The promising performance in both fields is demonstrated. In addition, we identify current limitations and propose future approaches for optimized materials design and OER/LIB performance. A simple two-step process starting from molecular vanadium oxide clusters embedded in a zeolitic imidazolate framework-67 (ZIF-67)[30] is used to access hierarchically structured composites where crystalline Co–V–oxide nanoparticles (~5 nm diameter) are embedded in a layered nitrogen-doped porous carbon matrix. When used as OER electrocatalyst, the composite shows excellent performance featuring low overpotential and small Tafel slopes. As test LIB anode, the composite combines high rate performance with long cycling stability. This new class of materials therefore paves the way for developing multifunctional composites based on one family of molecular precursors.

2.1. Synthesis and characterization

As shown in Scheme 1, the multifunctional composite is easily accessed by a scalable two-step fabrication process. Here, we used decavanadate anions $[H_3V_{10}O_{28}]^{3-}$ (=$\{V_{10}\}$) as molecular vanadium oxide precursor.[31] As MOF model, we employed ZIF-67 which is based on Co^{2+} ions linked by 2-methylimidazole ligands into a 3d porous framework. The **{V_{10}}@ZIF-67** composite was obtained by reaction of **{V_{10}}**, $Co(NO_3)_2 \times 6H_2O$ and 2-methylimidazole in methanol at room temperature ($t_{reaction}$ = 12 h). The solid samples were recovered by centrifugation, washed, dried and pyrolyzed in a tube furnace (480 °C; heating rate: 10 °C min^{-1}; N_2 atmosphere; t = 4 h), giving the final composite, hereafter referred to as **CoVO/C**. FT-IR, CHN elemental analysis and thermogravimetric analysis (TGA) were used to determine composition and purity of the products (see ESI, Fig. S1, S2 and Table S1†).

Scanning electron microscopy (SEM) and transmission electron microscopy (TEM) were used to characterize the nanostructure of **{V_{10}}@ZIF-67** and **CoVO/C**. SEM analysis shows that **{V_{10}}@ZIF-67** is obtained as distorted polyhedron (Fig. 1b) with similar morphology as the non-modified ZIF-67 rhombic dodecahedra (Fig. 1a). The distortion could be associated with the embedding of the **{V_{10}}** (diameter ~ 0.9 nm) within the ZIF-67 pore (~1.1 nm pore diameter).[12] In addition, the composite features smaller particle size (diameter ~ 100 nm) compared to the pure parent compound (diameter ~ 200 nm).

Thermogravimetric analyses (TGA) indicated 480 °C as a suitable pyrolysis temperature, since a thermally stable phase was obtained (Fig. S2 and S3†). After pyrolysis of **{V_{10}}@ZIF-67** at 480 °C, electron microscopy shows that a hierarchically porous composite is obtained (Fig. 1c–f and S3d, e†). The surface of the individual **CoVO/C** composite particles is rough and porous, possibly due to the formation of gaseous products during pyrolysis of the organic ZIF-67 components (Fig. 1c and d). In the **CoVO/C** composite, we observe homogeneously distributed metal oxide particles embedded in the carbon matrix (Fig. 1g and h). Further, powder X-ray diffraction (pXRD) shows the presence of the two crystalline Co–V–oxide phases $Co_3V_2O_8$ (JCPDS card no. 16-0675) and CoV_3O_8 (JCPDS card no. 22-0598, Fig. S4†).

Aberration-corrected high resolution TEM (AC-HR-TEM) indicates the presence of crystalline Co–V–oxide particles (diameter ~ 5 nm) embedded in a layered carbon matrix with layer spacing of *ca.* 0.34 nm. The corresponding lattice fringes are assigned to the (002) plane of graphitic carbon, see Fig. 1g and h.[32] The embedded cobalt vanadates (Fig. 1g, h and S3e†), possess well-defined crystallinity, several interlayer distances could be assigned to the corresponding Miller-planes observed by pXRD which are further identified by (AC-HR) TEM and pXRD, see Fig. 1g, h and S4.†[33]

X-ray photoelectron spectroscopy (XPS) of **CoVO/C** confirms the presence of Co, V, O and C and gives a Co–V–oxide content of ~57 wt% and C/N content of ~43% (Table S2†). As shown in Fig. S5,† the deconvoluted C 1s spectrum indicates the presence of O=C–O, C–O/C–N, and C=C/C–C/C–H species. The N 1s deconvoluted spectrum shows signals for pyrrolic and pyridinic nitrogen atoms, thereby indicating the nitrogen-doping of the carbonaceous matrix. The deconvoluted O 1s spectrum gives signals for metal oxide and C–O species. The vanadium spectral region shows three peaks assigned to V^{V} $2p_{1/2}$ (525.2 eV), V^{IV} $2p_{1/2}$ (523.8 eV), V^{V} $2p_{3/2}$ (517.7 eV) and V^{IV} $2p_{3/2}$ (516.2 eV).[34–36] The deconvoluted Co 2p spectrum features four peaks, which correspond to Co^{II} $2p_{1/2}$ (797.5 eV), Co^{III} $2p_{1/2}$ (796.0 eV), Co^{II} $2p_{3/2}$ (782.0 eV), and Co^{III} $2p_{3/2}$ (780.5 eV),[37–39] which is in line with the presence of $Co_3V_2O_8$ and CoV_3O_8 observed by pXRD.

As the accessible specific surface area is highly relevant for most electrochemical applications, nitrogen sorption (BET) was

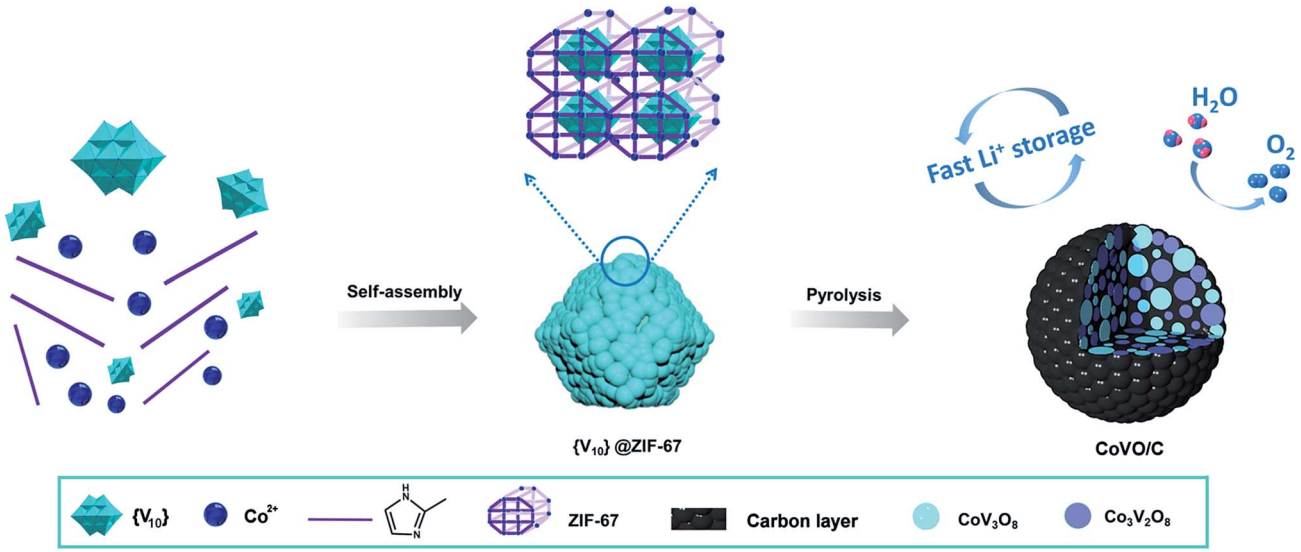

Scheme 1 Illustration of the two-step fabrication process of the **CoVO/C** composite.

used to examine the **CoVO/C** composite. The study shows that the composite features a high specific surface area (S_{BET} = 931 m^2 g^{-1}). In contrast, when non-modified ZIF-67 is pyrolyzed under identical conditions, significantly lower porosity (S_{BET} = 128 m^2 g^{-1}) is observed, highlighting that the incorporated **{V_{10}}** modifies the pore formation process[12,40] (Fig. S6†).

2.2. Oxygen evolution catalysis

Based on the known oxidative reactivity of Co-oxides, we examined the activity of **CoVO/C** drop-casted on glassy carbon electrodes for OER in a three-electrode setup using 1 M aqueous KOH as electrolyte (Experimental details see ESI†).[41] Linear sweep voltammetry (LSV, see Fig. 2a) indicates that **CoVO/C** shows high OER activity with an overpotential of 350 mV (at 10 mA cm^{-2}) and a Tafel slope of 75 mV dec^{-1} (Fig. 2b). In contrast, the pyrolyzed pure ZIF-67 reference shows significantly higher overpotentials (520 mV at 10 mA cm^{-2}) and Tafel slope (131 mV dec^{-1}). When compared with recent related OER electrocatalysts, we note that **CoVO/C** shows highly competitive performance (Table S4†).[42,43]

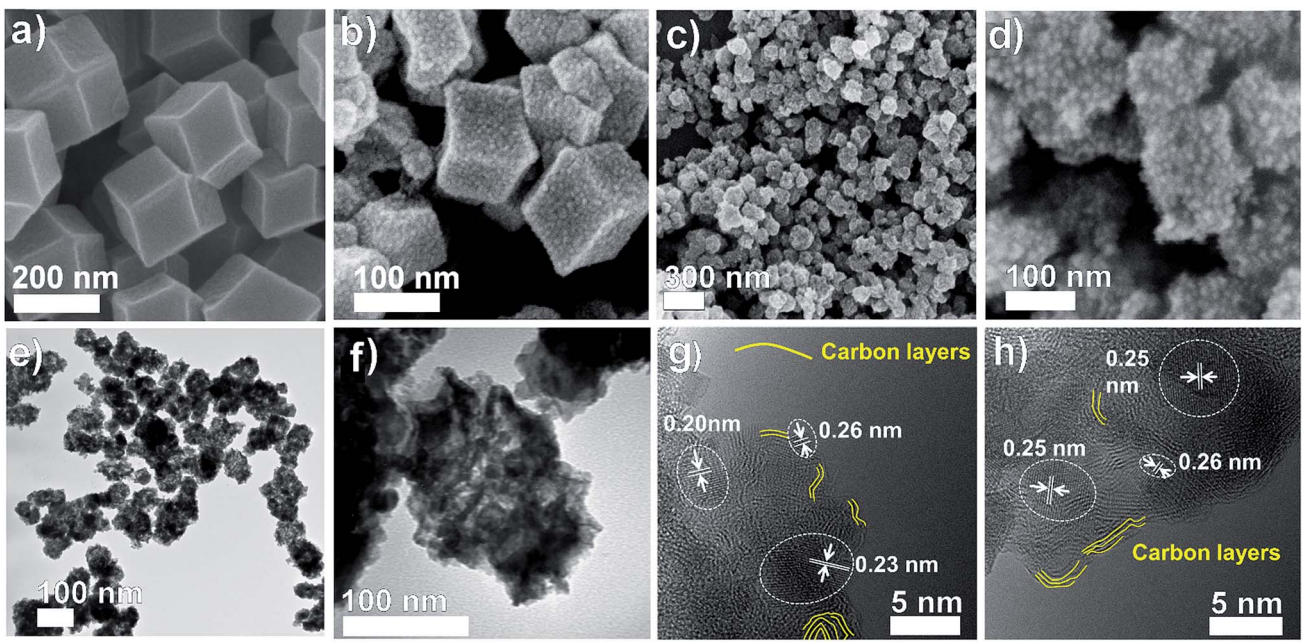

Fig. 1 SEM images of (a) non-modified ZIF-67 and (b) **{V_{10}}@ZIF-67**; SEM (c, d) and TEM (e, f) images of **CoVO/C** pyrolyzed at 480 °C; (g, h) (AC-HR) TEM images of as-prepared **CoVO/C**. The interlayer distances of 0.20 nm and 0.25 nm are assigned to the (400), (311) lattice planes of $Co_3V_2O_8$. The interlayer distances of 0.26 nm and 0.23 nm are assigned to the (303) and (114) lattice planes of CoV_3O_8 (see Fig. S4†).

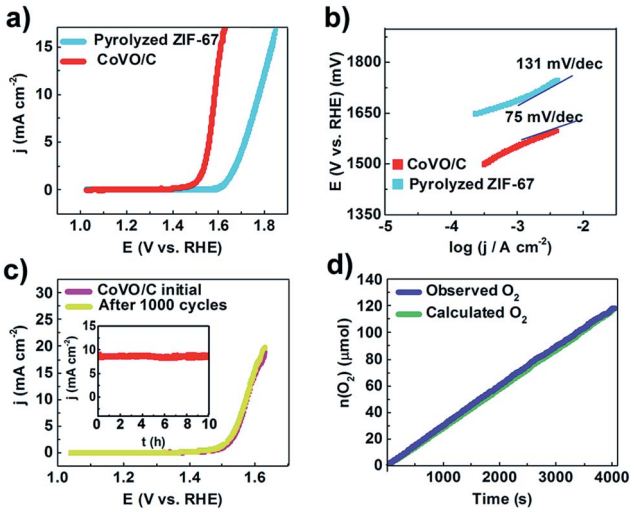

Fig. 2 (a) LSV polarization curves and (b) Tafel plots of **CoVO/C**, and the pyrolyzed ZIF-67 reference in 1.0 M aqueous KOH for the OER. (c) Polarization curves of **CoVO/C** before and after 1000 CV cycles. Inset: chronoamperometric data (E = 1.58 V) for **CoVO/C** over 10 h; (d) observed *vs.* calculated oxygen evolution showing the high faradaic OER efficiency (~100%) of **CoVO/C**.

The long-term stability of the **CoVO/C** electrode was examined by performing 1000 CV cycles between 0 and 1 V and no fading of the electrochemical response was observed. LSV analyses before and after the cycling (Fig. 2c) showed virtually identical traces so that no deterioration of the OER performance was observed. The long-term stability of the catalyst was tested by chronoamperometry at a potential of 1.58 V for 10 h. The study showed no drop of current density over this period and suggests high long-term stability under harsh chemical conditions (Fig. 2c, inset). The faradaic efficiency of the **CoVO/C** OER catalyst was quantified by determining the molar amount of oxygen evolved (using an oxygen sensitive fluorescence probe) while performing a bulk electrolysis at E = 1.58 V in deoxygenated 1 M aqueous KOH under a positive argon pressure (Fig. 2d). When comparing the observed O_2 amount with the theoretically calculated amount, we observe a faradaic efficiency of ~100%, highlighting the efficient OER performance of the composite.[44,45] Future development of this materials class needs to explore the performance under industrial conditions at high current densities (>0.5 A cm^{-2}) to understand performance limitations under these harsh conditions.

2.3. Lithium ion battery electrode

Next, we examined the performance of **CoVO/C** composite as lithium-ion battery anode in coin-type half cells (using Li metal as counter electrode). The working electrodes were composed of 80 wt% **CoVO/C** powder as active material, 10 wt% SuperC65 as conductive carbon and 10 wt% polyvinylidene fluoride as binder. Fig. S7† shows cyclic voltammetry (CV) profiles of the first six cycles, and multiple cathodic and anodic peaks can be observed in the first cycles, indicating multi-step electrochemical processes of the **CoVO/C**-based electrode. Importantly, apart from the initial scan, the subsequent cycles remain virtually identical, suggesting the stability of the electrode active material.[46]

Fig. 3a shows the long-term cycling performance of the **CoVO/C** electrode at a current density of 200 mA g^{-1} over 100 cycles. A low initial coulombic efficiency (~46%) is observed, which we associate with structural changes within the highly porous materials and possible contributions by irreversible lithiation processes.[47] However, upon longer cycling, the coulombic efficiency is >98% after cycle 50. Similarly, the 2nd to 7th cycle show slight fading of the specific capacity; however,

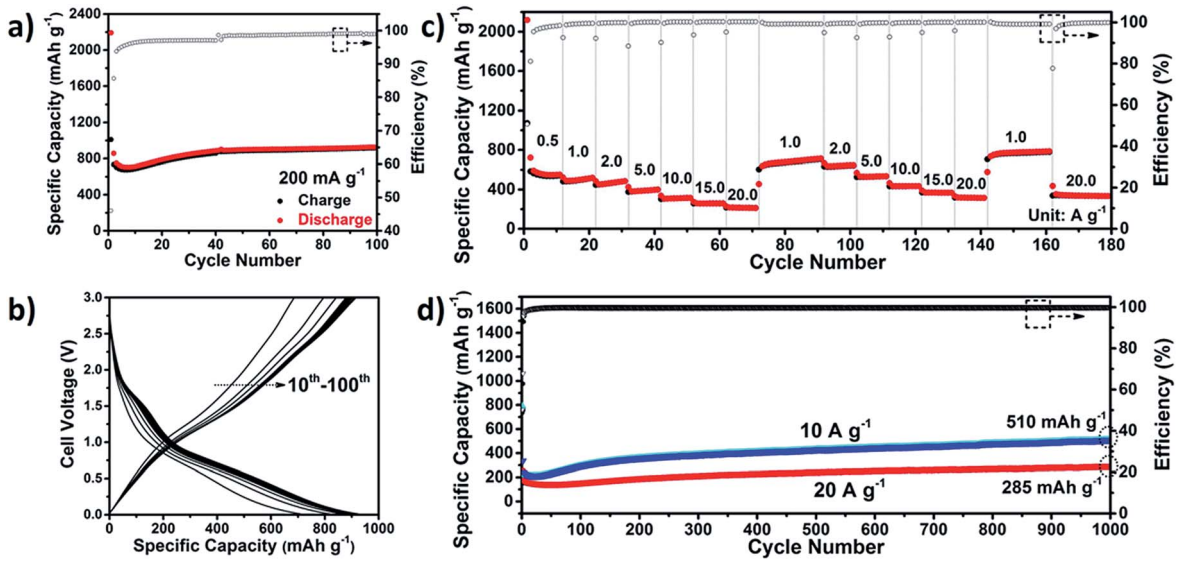

Fig. 3 Electrochemical performance of **CoVO/C** LIB anodes: (a) cycling performance at a current density of 200 mA g^{-1}; (b) corresponding discharge–charge profiles for selected cycles (cycle 10, 20,…100) at 200 mA g^{-1}; (c) rate performance at current densities from 0.5 to 20 A g^{-1}; (d) long-term cycling performance at high current densities (10 and 20 A g^{-1}).

gradual increase of the specific capacity is then observed until the 40th cycle where it reaches a plateau. After ~100 cycles, the electrode delivers a stable reversible specific capacity of ~920 mA h g^{-1}, accompanied by coulombic efficiencies >99%.[48,49] The high cycling stability of the electrode is confirmed by the corresponding voltage profiles (Fig. 3b) which remain virtually identical after cycle 60. Post-cycling *ex situ* SEM and TEM analyses of **CoVO/C** collected after 100 cycles (see Fig. S8†), show that the original porous structure has been covered by a uniform SEI layer (see Fig. S8a†). Also, the voids initially observed in the pristine material (see Fig. 1f) have disappeared (see Fig. S8b†), most likely due to the volumetric changes occurring during repeated (de)lithiation. This would be in line with the changes in specific capacity and coulombic efficiency described above.[47]

Further, we explored the rate capability of the **CoVO/C** electrode at current densities from 0.5 to 20 A g^{-1} (Fig. 3c and S9†). The electrodes showed excellent stability at all C-rates tested and gave specific capacities between 574 mA h g^{-1} (at 0.5 A g^{-1}) and 215 mA h g^{-1} (at 20 A g^{-1}). We note that upon cycling, the specific capacity of the electrode increases, see Fig. 3c. This indicates that structural changes within the electrode under operation could offer a facile approach to optimize electrochemical performance.

We further examined the electrode stability at high current densities of 10 and 20 A g^{-1} for 1000 cycles. Here, we observed remarkable cycling performance with final specific capacities of 510 mA h g^{-1} (at 10 A g^{-1}) and 285 mA h g^{-1} (at 20 A g^{-1}) after cycle 1000 (see Fig. 3d). Note that similar cobalt vanadium oxides have recently been studied as active materials in LIBs. For example, Lou *et al.* have synthesized Co_3O_4@$Co_3V_2O_8$ hollow nanocomposites, which exhibit a high reversible capacity of *ca.* 600 mA h g^{-1} after 500 cycles at 1 A g^{-1}.[50] For further comparison see Fig. S11 and Table S3.†

3. Conclusion

In conclusion, we report a convergent materials design approach to multi-functional electroactive metal oxide/carbon composites based on 3d transition metal-based molecular precursors. The integration of redox-active vanadium oxide clusters in a porous metal–organic framework and subsequent thermal conversion gives a hierarchically nanostructured Co–V–oxide/porous carbon composite with remarkable performance as oxygen evolution reaction electrocatalyst and potential lithium ion battery anode. The electrocatalytic oxygen evolution reaction performance under technologically relevant conditions in alkaline water electrolysis shows remarkable long-term stability and outstanding faradaic efficiency without loss of catalytic reactivity. The battery performance shows promising cycling stability, high specific capacity and high rate capability at charge/discharge rates up to 20 A g^{-1}. In future, this new design approach can in principle be transferred to a multitude of (mixed) metal oxide/carbon composites, so that a new class of multifunctional materials for electrochemical energy applications could become accessible. Work towards this end is currently underway.

4. Experimental section

4.1. Synthesis of $TBA_3[H_3V_{10}O_{28}]$ cluster (=TBA_3{V_{10}})

$TBA_3[H_3V_{10}O_{28}]$ was synthesized based on ref. 51 aqueous HCl (25.0 mL, 3 mol L^{-1}) was added drop by drop to an aqueous solution of Na_3VO_4 (5.00 g, 35.0 mL) under stirring. The orange solution was slowly added in an aqueous solution of (n-$C_4H_9)_4NBr$ (= TBABr, 20 g, 30 mL), resulting in the precipitation of a large amount of yellow-orange solid. The yellow precipitate was collected by suction filtration, washed successively with 20 mL of H_2O, 20 mL of ethanol, and 50 mL of ether, and finally dried for 3 h under vacuum to give 3.5 g of yellow-orange solid. The crude material was purified by recrystallization from CH_3CN using diethyl ether diffusion. The yellow-orange crystals were collected by suction filtration, washed with ether, and dried overnight under vacuum to give 1.0 g (22% based on V) of yellow-orange solid.

4.2. Synthesis of ZIF-67

The synthesis of ZIF-67 was based on ref. 52 a methanolic solution (80 mL) of $CoCl_2 \times 2H_2O$ (519 mg, 3.1 mmol) and 2-methylimidazole ($C_4H_6N_2$) (2.63 g, 32.0 mmol) were mixed under stirring. The mixture was stirred at room temperature for 12 h. The bright purple powder formed (ZIF-67) was collected by centrifugation, washed several times with methanol, and dried at 80 °C.

4.3. Synthesis of {V_{10}}@ZIF-67 composites

40 mL methanolic solution of $CoCl_2 \times 2H_2O$ (519 mg, 3.1 mmol) and $TBA_3[H_3V_{10}O_{28}]$ (25 mg, 0.015 mmol) was prepared under stirring and added to 40 mL of methanolic solution of 2-methylimidazole ($C_4H_6N_2$) (2.63 g, 32.0 mmol), followed by stirring. After 10 h of stirring, a dark purple powder of **{V_{10}}@ZIF-67** was collected by centrifugation, washed several times with methanol, and dried at 80 °C.

4.4. Synthesis of CoVO/C nanocomposites

{V_{10}}@ZIF-67 powder was transferred into a tube furnace in a porcelain boat and pyrolyzed at 480 °C under N_2 atmosphere for 4 h (heating ramp: 10 °C min^{-1}).

4.5. Control experiment

Pristine ZIF-67 powder and **{V_{10}}@ZIF-67** powder were transferred into a tube furnace in two separate porcelain boats and pyrolyzed at 280 °C under N_2 atmosphere for 4 h (heating ramp: 10 °C min^{-1}). (TEM images of both products can be seen in Fig. S3a and b†) a portion of **{V_{10}}@ZIF-67** powder was transferred into a tube furnace in a porcelain boat and pyrolyzed at 400 °C under N_2 atmosphere for 4 h (heating ramp: 10 °C min^{-1}). (TEM image of the product can be seen in Fig. S3c†).

4.6. Electrocatalytic oxygen evolution

Electrochemical measurements were performed in a standard three electrode system controlled by an electrochemical

workstation (CHI730, CH Instruments) with a glassy carbon rotating disk electrode (RDE) as the working electrode, saturated Ag/AgCl as the reference electrode, and a Pt mesh as counter electrode. All electrodes were equilibrated in O_2-saturated aqueous KOH solution (1 M) for 30 min prior to use. The working electrodes were prepared by dispersing the respective composites (3 mg) in EtOH (1 mL) by sonication (30 min). Then 12.6 μL of the catalyst ink was loaded onto a GC rotating disk electrode (RDE) of 4 mm diameter (the loading of catalyst was 0.3 mg cm^{-2}). After drying, the electrode was coated with a thin Nafion film by dropping 1.0 μL 0.5 wt% Nafion solution (solvent: isopropanol) onto its surface. The potential of the reference electrode was converted to RHE according to the Nernst equation ($E_{RHE} = E_{Ag/AgCl} + E^0_{Ag/AgCl} + 0.059$ pH, pH (based on activity) = 13.8). Prior to electrochemical analysis, the catalyst was pre-conditioned by 100 cyclic voltammetry scans (0–1 V, scan rate = 100 mV s^{-1}). Electrode polarization curves were obtained by linear sweep voltammetry at a scan rate of 5 mV s^{-1}. All polarization curves were corrected for IR losses unless noted otherwise. Chronoamperometry was performed at 1.58 V (*vs.* RHE) in an O_2-saturated aqueous KOH solution (1 M). Oxygen evolution measurements were carried out using a CH Instruments CHI730 potentiostat using **CoVO/C** on carbon fibre paper (size: 1 × 4 cm^2) as working electrode, a Pt mesh counter electrode and an Ag/AgCl reference electrode. To prepare the working electrode, 0.3 mg catalyst was dispersed in 2 mL EtOH followed by sonication for 30 min. The catalyst ink (150 μL) was drop-coated onto carbon fibre paper (1 × 1 cm^2 loaded area) and allowed to air-dry. After drying, the electrode was coated with a thin Nafion film by dropping 10 μL 0.5 wt% Nafion solution onto its surface. Experiments were carried out in an argon-filled glove bag in de-gassed aqueous 1.0 M KOH solution. Oxygen evolution was followed using a Pyro Science FireSting optical oxygen sensor. The charge flow and oxygen evolution were recorded, and theoretical and experimental molar amounts of oxygen evolution were calculated as follows:

$$n_{O_2}(\text{theoretical}) = \frac{Q}{4F}$$

$$n_{O_2}(\text{experimental}) = \frac{PV}{RT} = \frac{P\left(V_{(\text{cell})} - V_{(\text{electrolyte})}\right)}{RT}$$

$$\eta = \frac{n_{O_2}(\text{experimental}) + c_{(\text{solu.}O_2)}V_{(\text{electrolyte})}}{n_{O_2}(\text{theoretical})} \times 100\%$$

4.7. LIB characterization

The electrochemical performance of **CoVO/C** was measured using stainless steel 2032 coin cells with lithium metal (Rockwood Lithium, battery grade) as counter electrode. The working electrodes (WE) were composed of 80 wt% **CoVO/C** powder as active material, 10 wt% SuperC65 (TIMCAL) as conductive carbon and 10 wt% polyvinylidene fluoride (PVdF) as binder. For the WE preparation, PVdF powder was dissolved in *N*-methylpyrrolidinone (NMP, Sigma-Aldrich) to get a 10 wt% solution. Then, the **CoVO/C** powder and SuperC65 were added and the suspension was stirred overnight. The resulting homogeneous black slurry was spread onto copper foil (SCHLENK, 99.9%) using doctor blading with a wet film thickness of 120 μm. As-obtained electrodes were dried at 60 °C overnight, subsequently punched into 12 mm diameter and vacuum-dried for 24 h at 120 °C. The mass loading of the active materials was 0.9–1.2 mg cm^{-2}. The WE and lithium metal (counter electrode) were separated by a sheet of glass fiber (GF/D, Whatman) as separator. The electrolyte (UBE) was 1 mol L^{-1} $LiPF_6$ in ethylene carbonate/diethyl carbonate (EC/DEC, 1 : 1 v/v) solution with 1 vol% vinylene carbonate (VC). 2-Electrode 2032-type coin cells were assembled in a glove box (MBraun UNIlab; O_2 and H_2O content < 0.1 ppm). All electrochemical measurements were performed at 20 ± 2 °C. The galvanostatic (dis-)charge experiments were performed using a Maccor 3000 battery tester, with the voltage range of 0.01–3.0 V. Cyclic voltammetry (CV) was conducted using a VMP3 potentiostat (Bio-Logic Science Instruments) in the same potential range, *i.e.*, 0.01–3.0 V.

Conflicts of interest

There are no conflicts to declare.

Acknowledgements

Y. J., R. L., K. C., U. K. and C. S. acknowledge financial support by the Deutscher Akademischer Austauschdienst DAAD, Deutsche Forschungsgemeinschaft DFG (TRR234 CataLight, projects B3 and C4, STR1164/12), and Ulm University. Y. M., Y.-J. M. and K. C. acknowledge financial support from the Chinese Scholarship Council (CSC). R. L. acknowledges the Alexander-von-Humboldt-Foundation for a postdoctoral fellowship. A. V., and S. P. acknowledge financial support from the Helmholtz Association and Karlsruher Institute of Technology. Y.-F. S. acknowledges the National Natural Science Foundation of China. Dr Thomas Diemant is acknowledged for XPS measurement. Prof. Dr Paul Walther is acknowledged for TEM access.

Notes and references

1 M. Oh, T. Yu, S. Yu, B. Lim, K. Ko, M. Willinger, D. Seo and B. Kim, *Science*, 2013, **340**, 964–968.
2 H. Bin Wu and X. W. Lou, *Sci. Adv.*, 2017, **3**, 1–17.
3 R. Schmuch, R. Wagner, G. Hörpel, T. Placke and M. Winter, *Nat. Energy*, 2018, **3**, 267–278.
4 M. Martin-Sabi, J. Soriano-López, R. S. Winter, J. J. Chen, L. Vilà-Nadal, D. L. Long, J. R. Galán-Mascarós and L. Cronin, *Nat. Catal.*, 2018, **1**, 208–213.
5 D. N. Mueller, M. L. MacHala, H. Bluhm and W. C. Chueh, *Nat. Commun.*, 2015, **6**, 1–8.
6 A. Grimaud, O. Diaz-Morales, B. Han, W. T. Hong, Y. L. Lee, L. Giordano, K. A. Stoerzinger, M. T. M. Koper and Y. Shao-Horn, *Nat. Chem.*, 2017, **9**, 457–465.

7 Y. Nishimoto, D. Yokogawa, H. Yoshikawa, K. Awaga and S. Irle, *J. Am. Chem. Soc.*, 2014, **136**, 9042–9052.
8 L. A. W. Ellingsen, C. R. Hung, G. Majeau-Bettez, B. Singh, Z. Chen, M. S. Whittingham and A. H. Strømman, *Nat. Nanotechnol.*, 2016, **11**, 1039–1051.
9 N. I. Gumerova and A. Rompel, *Nat. Rev. Chem.*, 2018, **2**, 0112.
10 J. Yang, F. Zhang, X. Wang, D. He, G. Wu, Q. Yang, X. Hong, Y. Wu and Y. Li, *Angew. Chem., Int. Ed.*, 2016, **55**, 12854–12858.
11 Y. Ji, L. Huang, J. Hu, C. Streb and Y. Song, *Energy Environ. Sci.*, 2015, **8**, 776–789.
12 M. Stuckart and K. Y. Monakhov, *J. Mater. Chem. A*, 2018, **6**, 17849–17853.
13 L. Cronin and A. Müller, *Chem. Soc. Rev.*, 2012, **41**, 7325–7648.
14 Y. Ji, J. Hu, J. Biskupek, U. Kaiser, Y. F. Song and C. Streb, *Chem.–Eur. J.*, 2017, **23**, 16637–16643.
15 L. E. Vangelder, A. M. Kosswattaarachchi, P. L. Forrestel, T. R. Cook and E. M. Matson, *Chem. Sci.*, 2018, **9**, 1692–1699.
16 C. Streb, *Structure and Bonding in Molecular Vanadium Oxides: From Templates via Host–Guest Chemistry to Applications*, Springer Verlag, Berlin, Heidelberg, 2017, pp. 1–17.
17 K. Y. Monakhov, W. Bensch and P. Kögerler, *Chem. Soc. Rev.*, 2015, **44**, 8443–8483.
18 K. Kastner, J. T. Margraf, T. Clark and C. Streb, *Chem.–Eur. J.*, 2014, **20**, 12269–12273.
19 K. Kastner, J. Forster, H. Ida, G. N. Newton, H. Oshio and C. Streb, *Chem.–Eur. J.*, 2015, **21**, 7686–7689.
20 K. Kastner, M. Lechner, S. Weber and C. Streb, *ChemistrySelect*, 2017, **2**, 5542–5544.
21 M. H. Anjass, K. Kastner, F. Nägele, M. Ringenberg, J. F. Boas, J. Zhang, A. M. Bond, T. Jacob and C. Streb, *Angew. Chem., Int. Ed.*, 2017, **56**, 14749–14752.
22 B. Schwarz, J. Forster, M. K. Goetz, D. Yücel, C. Berger, T. Jacob and C. Streb, *Angew. Chem., Int. Ed.*, 2016, **55**, 6329–6333.
23 F. Li, S. H. Carpenter, R. F. Higgins, M. G. Hitt, W. W. Brennessel, M. G. Ferrier, S. K. Cary, J. S. Lezama-Pacheco, J. T. Wright, B. W. Stein, M. P. Shores, M. L. Neidig, S. A. Kozimor and E. M. Matson, *Inorg. Chem.*, 2017, **56**, 7065–7080.
24 S. Mukhopadhyay, J. Debgupta, C. Singh, A. Kar and S. K. Das, *Angew. Chem., Int. Ed.*, 2018, **57**, 1918–1923.
25 G. Paille, M. Gomez-Mingot, C. Roch-Marchal, B. Lassalle-Kaiser, P. Mialane, M. Fontecave, C. Mellot-Draznieks and A. Dolbecq, *J. Am. Chem. Soc.*, 2018, **140**, 3613–3618.
26 C. Freire, D. M. Fernandes, M. Nunes and V. K. Abdelkader, *ChemCatChem*, 2018, **10**, 1703–1730.
27 D. Y. Du, J. S. Qin, S. L. Li, Z. M. Su and Y. Q. Lan, *Chem. Soc. Rev.*, 2014, **43**, 4615–4632.
28 H. Bin Wu, B. Y. Xia, L. Yu, X. Yu and X. W. Lou, *Nat. Commun.*, 2015, **6**, 6512.
29 S. Niu, Z. Wang, T. Zhou, M. Yu, M. Yu and J. Qiu, *Adv. Funct. Mater.*, 2017, **27**, 1605332.
30 O. M. Yaghi, *Science*, 2008, **319**, 939–943.
31 M. H. Anjass, M. Deisböck, S. Greiner, M. Fichtner and C. Streb, *ChemElectroChem*, 2018, **6**, 398–403.
32 W. Zhang, X. Jiang, X. Wang, Y. V. Kaneti, Y. Chen, J. Liu, J. Sen Jiang, Y. Yamauchi and M. Hu, *Angew. Chem., Int. Ed.*, 2017, **56**, 8435–8440.
33 F.-C. Shen, Y. Wang, Y.-J. Tang, S.-L. Li, Y.-R. Wang, L.-Z. Dong, Y.-F. Li, Y. Xu and Y.-Q. Lan, *ACS Energy Lett.*, 2017, **2**, 1327–1333.
34 G. H. Jeong, I. Lee, D. Lee, H.-M. Lee, S. Baek, O.-P. Kwon, P. N. Kumta, S. Yoon and S.-W. Kim, *Nanotechnology*, 2018, **29**, 195403.
35 Y. Zhao, Y. Liu, X. Du, R. Han and Y. Ding, *J. Mater. Chem. A*, 2014, **2**, 19308–19314.
36 H.-Y. Chen, G. Wee, R. Al-Oweini, J. Friedl, K. S. Tan, Y. Wang, C. L. Wong, U. Kortz, U. Stimming and M. Srinivasan, *ChemPhysChem*, 2014, **15**, 2162–2169.
37 Y. Zhai, H. Mao, P. Liu, X. Ren, L. Xu and Y. Qian, *J. Mater. Chem. A*, 2015, **3**, 16142–16149.
38 G. Yang, H. Cui, G. Yang and C. Wang, *ACS Nano*, 2014, **8**, 4474–4487.
39 V. Soundharrajan, B. Sambandam, J. Song, S. Kim, J. Jo, S. Kim, S. Lee, V. Mathew and J. Kim, *ACS Appl. Mater. Interfaces*, 2016, **8**, 8546–8553.
40 M. Zhang, A. M. Zhang, X. X. Wang, Q. Huang, X. Zhu, X. L. Wang, L. Z. Dong, S. L. Li and Y. Q. Lan, *J. Mater. Chem. A*, 2018, **6**, 8735–8741.
41 W. Luo, J. Hu, H. Diao, B. Schwarz, C. Streb and Y. F. Song, *Angew. Chem., Int. Ed.*, 2017, **56**, 4941–4944.
42 R. Liu, G. Zhang, H. Cao, S. Zhang, Y. Xie, A. Haider, U. Kortz, B. Chen, N. S. Dalal, Y. Zhao, L. Zhi, C. X. Wu, L. K. Yan, Z. Su and B. Keita, *Energy Environ. Sci.*, 2016, **9**, 1012–1023.
43 Y. Chen, J. Hu, H. Diao, W. Luo and Y. F. Song, *Chem.–Eur. J.*, 2017, **23**, 4010–4016.
44 W. Luo, J. Wang, J. Hu, Y. Ji, C. Streb and Y. F. Song, *ChemElectroChem*, 2018, **5**, 2850–2856.
45 R. Liu, H. Liu, Y. Li, Y. Yi, X. Shang, S. Zhang, X. Yu, S. Zhang, H. Cao and G. Zhang, *Nanoscale*, 2014, **6**, 11336–11343.
46 Y. Ma, Y. Ma, D. Geiger, U. Kaiser, H. Zhang, G. T. Kim, T. Diemant, R. J. Behm, A. Varzi and S. Passerini, *Nano Energy*, 2017, **42**, 341–352.
47 Y. Ma, Y. Ma, D. Bresser, Y. Ji, D. Geiger, U. Kaiser, C. Streb, A. Varzi and S. Passerini, *ACS Nano*, 2018, **12**, 7220–7231.
48 Y. Ma, U. Ulissi, D. Bresser, Y. Ma, Y. Ji and S. Passerini, *Electrochim. Acta*, 2017, **258**, 535–543.
49 Y. Ma, Y. Ma, U. Ulissi, Y. Ji, C. Streb, D. Bresser and S. Passerini, *Electrochim. Acta*, 2018, **277**, 100–109.
50 Y. Lu, L. Yu, M. Wu, Y. Wang and X. W. D. Lou, *Adv. Mater.*, 2018, **30**, 1702875.
51 V. W. Day, W. G. Klemperer and D. J. Maltbie, *J. Am. Chem. Soc.*, 1987, **109**, 2991–3002.
52 J. Tang, R. R. Salunkhe, J. Liu, N. L. Torad, M. Imura, S. Furukawa and Y. Yamauchi, *J. Am. Chem. Soc.*, 2015, **137**, 1572–1580.

